

Quantum metrological capability as a probe for quantum phase transition

Xiangbei Li,¹ Yaoming Chu,^{1,*} Shaoliang Zhang,¹ and Jianming Cai^{1,†}

¹*School of Physics, Hubei Key Laboratory of Gravitation and Quantum Physics,
International Joint Laboratory on Quantum Sensing and Quantum Metrology,
Institute for Quantum Science and Engineering,
Huazhong University of Science and Technology, Wuhan 430074, China*

Abstract

The comprehension of quantum phase transitions (QPTs) is considered as a critical foothold in the field of many-body physics. Developing protocols to effectively identify and understand QPTs thus represents a key but challenging task for present quantum simulation experiments. Here, we establish a dynamical quench-interferometric framework to probe a zero-temperature QPT, which utilizes the evolved state by quenching the QPT Hamiltonian as input of a unitary interferometer. The metrological capability quantified by the quantum Fisher information shows a unique peak in the vicinity of the quantum critical point, allowing us to probe the QPT without cooling the system to its ground state. We show that the probing can be implemented by extracting quantum fluctuations of the interferometric generator as well as parameter estimation uncertainty of the interferometric phase, and subsequently allows identifying the boundary of the phase diagram. Our results establish an important link between QPTs and quantum metrology, and enrich the toolbox of studying non-equilibrium many-body physics in current quantum simulators.

Introduction

Quantum phase transitions (QPTs) represent a vigorous subject strongly relevant in various fields, ranging from condensed matter to quantum field theory and cosmology [1, 2]. It is commonly considered an essential ingredient for our perception of a plethora of fascinating quantum phenomena in strongly correlated many-body physics such as quantum magnetization [3], spin liquid [4], topological order [5] and superconductor-insulator transition [6]. In the last few years, the booming development of AMO physics and quantum simulation technologies opens a pristine and versatile experimental avenue towards the study of QPTs through controllable realizations of a variety of theoretical models [7–13]. This also naturally inspires intensive attention of synergistically investigating QPTs in quantum simulators beyond the traditional Landau-Ginzburg paradigm, by resorting to the concepts and strategies developed in quantum information science [14–18].

Remarkably, a quantum-fidelity approach to QPTs has been put forward to unveil sharp variations of the ground state close to critical point from a universal information-theoretic picture [15, 16, 19–21]. However, the requirement of cooling a complex many-body system to nearly zero temperature might be challenging. More recently, frameworks based on non-equilibrium dynamical response after sudden quantum quenches interestingly demonstrate the possibility of establishing a versatile toolbox for locating and witnessing QPTs [22–34], and are expected to become a routine practice. While being compelling, efficient extraction of the quantities that act as indicators of the QPTs in those previous frameworks, such as short-range correlations [22, 23], out-of-time-order correlators [24, 25], entanglement entropy [23] and even multi-site entanglement [28], typically requires the ability of implementing local measurements or other complex operations (e.g. time-reversed evolution) on a generic many-body system. Therefore, further strengthening and enriching the toolbox of probing QPTs with quantum information strategies still remains largely unexplored and deserves intense efforts.

In this Letter, we establish an efficient framework for probing QPTs by integrating nonequilibrium quench dynamics with the concept of interferometry in quantum metrology. Specifically, we consider the post-quenched state prepared by time evolution governed by a QPT Hamiltonian as input of a unitary interferometer. We stress that our interferometric framework is different from the typical scenarios of critical metrology, which focus on estimating the QPT’s control parameter that drives the phase transition [19, 35–39]. The *metrological capability* of the state, theoretically quantified by the quantum Fisher information, determines the ultimate precision of estimating the interferometric phase. As our main result, we find that the metrological capability interest-

ingly shows a peak around the quantum critical point (QCP). We further demonstrate that this enhanced metrological capability can be effectively accessed through quantum fluctuation of the interferometric generator or the estimation uncertainty of the phase, which merely requires the measurement of certain collective spin operators by global detection of the QPT system. As a direct application, we obtain the boundary of the QPT phase diagram and show that it coincides well with the theoretical prediction of equilibrium QCPs. Our framework not only provides a new promising and experimentally practical avenue to investigate QPTs and the comprehension of non-equilibrium many-body quantum phenomena, but also reveals further deep connections between quantum metrology and quantum criticality [35–53].

Quench-interferometric framework for probing QPTs

At the heart of quantum metrology lies the quantum Fisher information (QFI) [54–56], which can quantify the metrological capability of a probe state with respect to the unitary parameterization generated by a Hermitian operator \hat{O} . In this work, we focus on the standard interferometric framework [41, 57–60], where a local N -particle generator $\hat{O} = \sum_{i=1}^N \hat{O}_i$ is considered. Given a pure probe state $|\Psi\rangle$, the associated QFI can be easily computed or measured from quantum fluctuation of the generator [56, 60]

$$F_Q[|\Psi\rangle, \hat{O}] = 4 \left[\langle \Psi | \hat{O}^2 | \Psi \rangle - \langle \Psi | \hat{O} | \Psi \rangle^2 \right]. \quad (1)$$

This form of QFI is elegantly linked to the connected correlation function, resulting in significant implications well beyond the scope of quantum metrology. Recently, in paradigmatic spin models of QPTs, it has been demonstrated that the QFI of the ground state can exhibit superextensive divergence or abrupt changes in the vicinity of a QCP [41, 60, 61]. Such fundamentally interesting behaviors could unveil a variety of fascinating phenomena such as the witness of critical multipartite entanglement [60], the redistribution of quantum noise among extensive observables [41] and the emergence of many-body nonlocality [61], which however is hindered by the requirement of ground state preparation.

Here, we consider the QFI of a probe state prepared through nonequilibrium quantum dynamics by suddenly quenching the QPT Hamiltonian, thus circumventing the challenging preparation of a many-body system near its ground state. It is worth to remark that the time-dependent QFI evolution in quench dynamics might open new possibilities beyond the knowledge of quantum systems at equilibrium, enabling alternative pathways towards various intriguing phenomena such as entangling dynamics [47, 49, 62–65], transient quantum coherence [66, 67] and the interplay between

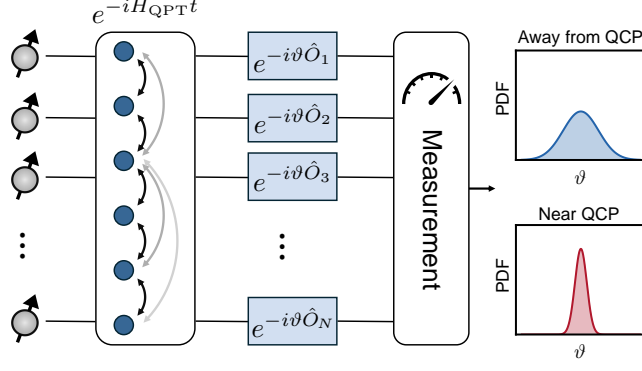


FIG. 1. **Schematic graph of the quench-interferometric framework for probing QPTs.** A many-body system of N particles is prepared into a probe state via nonequilibrium quantum dynamics, achieved by suddenly quenching the QPT Hamiltonian H_{QPT} . This probe state is then used to estimate an unknown phase ϑ encoded by a local generator $\hat{O} = \sum_{i=1}^N \hat{O}_i$. The metrological capability of the probe state can be significantly enhanced when the quenched Hamiltonian approaches the quantum critical point, as evidenced by a much narrower probability density function (PDF) of the estimated value of ϑ .

equilibrium and dynamical QCPs [22]. Explicitly, our study proposes a quench-interferometric framework that employs post-quenched states as input of interferometers, namely

$$|\Psi_t(\vartheta)\rangle = e^{-i\vartheta \hat{O}} e^{-iH_{\text{QPT}}t} |\Psi_0\rangle. \quad (2)$$

We firstly evolve the system to a probe state by a QPT Hamiltonian, i.e. $|\Psi_t\rangle = e^{-iH_{\text{QPT}}t} |\Psi_0\rangle$, and then input it into a quantum interferometer with a phase unitarily encoded by $e^{-i\vartheta \hat{O}}$, see Fig. 1. The ultimate measurement precision of the interferometric phase ϑ is determined by the QFI in $|\Psi_t(\vartheta)\rangle$, which is uniformly (namely, independent of ϑ) given by $F_Q(t) = F_Q[|\Psi_t\rangle, \hat{O}]$.

Below, we investigate identification of the QPT by analyzing QFI evolution of the post-quenched state in Eq. (2). As an illustrative example, we focus on the zero-temperature paramagnetic-to-ferromagnetic QPT embedded in the anisotropic next-nearest-neighbor Ising (ANNNI) chain, see Fig. 2(a), which is a representative model describing generic (quantum chaotic) many-body systems [23, 68]. The model Hamiltonian reads,

$$H(\kappa, B) = -J \sum_{i=1}^N \sigma_i^x \sigma_{i+1}^x + \kappa \sum_{i=1}^N \sigma_i^x \sigma_{i+2}^x - B \sum_{i=1}^N \sigma_i^z, \quad (3)$$

where $\sigma_i^{x,z}$ are the Pauli operators at site i , and a periodic boundary condition is employed with $\sigma_{N+1}^x = \sigma_1^x$, $\sigma_{N+2}^x = \sigma_2^x$. We set $J = 1$ in the following for simplicity. This model is generally

nonintegrable [68, 69] except for the special scenario of $\kappa = 0$. Second-order perturbation theory determines the paramagnetic-to-ferromagnetic transition line of the ANNNI chain as $1 - 2\kappa_c = B_c - \kappa_c B_c^2 / (2 - 2\kappa_c)$ [70]. In our framework, we initialize this spin chain in a fully polarized state $|\Psi_0\rangle = |\uparrow\rangle^{\otimes N}$ and let it evolve under the ANNNI Hamiltonian, i.e.

$$|\Psi_t\rangle = e^{-iH(\kappa, B)t} |\Psi_0\rangle. \quad (4)$$

We consider the collective spin operator $\hat{\mathcal{O}} = \hat{S}_x = \sum_{i=1}^N \sigma_i^x / 2$ as the phase-translation generator. Numerical calculations of $F_Q(t) = F_Q[|\Psi_t\rangle, \hat{S}_x]$ for 20 spins are performed using the exact diagonalization (ED) method [71, 72]. In Fig. 2 (b-c), we demonstrate that the QFI evolution of $|\Psi_t\rangle$ prepared by non-equilibrium quench dynamics in Eq. (4) can be employed to probe the QPT. It can be seen in Fig. 2 (b) that the QFI dynamics close to the QCP is radically enhanced in contrast to the scenarios away from the QCP. The averaged QFI is calculated over a time window of T to quantify the overall difference across the critical point, i.e.

$$\overline{F_Q} = (1/T) \int_0^T F_Q(t) dt. \quad (5)$$

Remarkably, $\overline{F_Q}$ displays a peak in the vicinity of the QCP as shown in Fig. 2 (c), which serves an effective indicator to locate the QPT. We note that the emergence of such a peak can be related to the spontaneous symmetry breaking [73]. Our numeric analysis also shows that these results are robust to a finite system size and open boundary condition [73].

Probing QPTs by global quantum fluctuations

The quantum fluctuations of the generator, defined as $\text{Var}[\hat{\mathcal{O}}] = \langle \Psi | \hat{\mathcal{O}}^2 | \Psi \rangle - \langle \Psi | \hat{\mathcal{O}} | \Psi \rangle^2$, are proportional to the QFI [see Eq. (1)]. It thus reflects the metrological capability of the post-quenched state. Therefore, a direct probing of QPTs via the metrological capability can be implemented by the measurement of $\hat{\mathcal{O}}$ (e.g. \hat{S}_x in ANNNI example) with respect to the post-quenched state $|\Psi_t\rangle$. For a measurement repetitions of m times, one obtains a series of random outcomes $\{S_x^{(1)}, S_x^{(2)}, \dots, S_x^{(m)}\}$ taking (half-)integer values in $[-N/2, N/2]$. The fluctuations of \hat{S}_x can be efficiently estimated using the Bessel Formula,

$$\text{Var}[\hat{S}_x] = \frac{1}{m-1} \sum_{i=1}^m \left(S_x^{(i)} - \langle \hat{S}_x \rangle \right)^2, \quad (6)$$

where $\langle \hat{S}_x \rangle = \sum_{i=1}^m S_x^{(i)} / m$. As demonstrated in Fig. 2(d), the measurement outcomes near the QCP apparently satisfy a wider probability distribution than the non-critical case. We calculate the

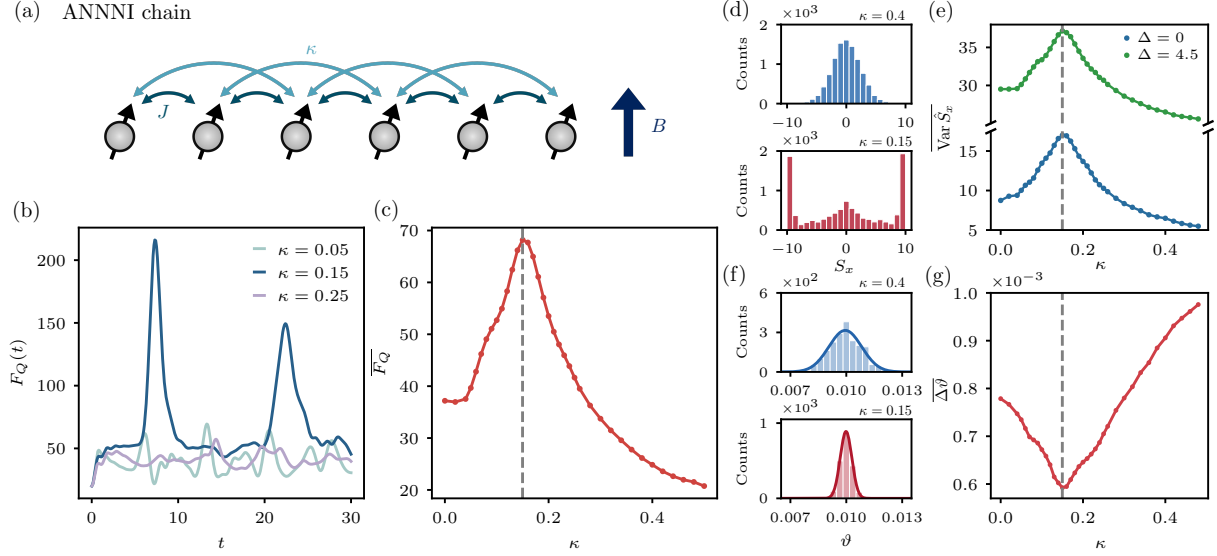


FIG. 2. **Probing the zero-temperature QPT of the ANNNI model.** (a) The ANNNI chain consists of nearest-neighboring and next-nearest-neighboring Ising interaction as well as a transverse biased field, denoted by the parameters (J, κ, B) respectively. In our simulation we set $J = 1$ and $B = 0.75$, which leads to a QCP at $\kappa_c \approx 0.15$ marked by the vertical dashed gray lines in the following panels. (b) The QFI dynamics for different values of κ . The apparently enhanced QFI (dark blue curve) corresponds to the quench parameter κ close to the QCP. (c) The time-averaged QFI exhibits a maximum in the vicinity of the QCP. (d) Histogram of $m = 10000$ simulated measurement outcomes of \hat{S}_x on the posted-quenched state at $t = 7.5$. (e) The time average of quantum fluctuations in Eq. (6) is obtained for different measurement resolutions. They all show a peak that coincides well with the equilibrium QCP. (f) Histogram of 2000 simulated MLE of the interferometric phase using the posted-quenched state at $t = 7.5$. The solid lines represent the Gaussian fitting centered around the true value $\vartheta = 0.01$. (g) Time-averaged uncertainty of MLE estimate, see Eq. (8), identifies the QCP by its minimum. Here, the system size is set as $N = 20$ and the window of the time-averaging operation is chosen as $T = 15$.

time-averaged fluctuations $\overline{\text{Var} \hat{S}_x} = (1/T) \int_0^T \text{Var}[\hat{S}_x] dt$, which evidently shows a peak versus the quench parameter κ around the QCP, see Fig. 2(e).

To account for the influence of a limited experimental measurement resolution that technically coarsens the measurement outcomes, the outcome $S_x^{(i)}$ for the i -th measurement can be assumed to be continuously distributed, with the corresponding measurement operator given by [55, 73–75]

$$\hat{\Pi}(S_x^{(i)}) = \frac{1}{\sqrt{2\pi}\Delta} e^{-(S_x^{(i)} - \hat{S}_x)^2 / (2\Delta^2)}. \quad (7)$$

The standard deviation Δ effectively quantifies the measurement resolution, and when $\Delta \rightarrow 0$, Eq. (7) recovers the ideal projective measurement $\hat{\Pi}(S_x^{(i)}) = \delta(S_x^{(i)} - \hat{S}_x)$ with $\delta(x)$ denoting the Dirac delta function. We numerically simulate the measurement process of \hat{S}_x under different resolutions and then evaluate quantum fluctuation based on Eq. (6). In Fig. 2 (e), we depict the time-averaged $\overline{\text{Var} \hat{S}_x}$ versus the quench parameter κ . Our results shows that the position of the peak at QCP is not influenced even for a poor measurement resolution of $\Delta \sim \sqrt{N} \approx 4.5$, which would facilitate the observable $\text{Var}[\hat{S}_x]$ to function as a trustworthy probe of QPTs.

Probing QPTs by estimation uncertainty

Naturally, the quantum probe state with a larger metrological capability gives to a better precision in estimating the phase ϑ associated with the unitary parameterization, i.e., $|\Psi_t(\vartheta)\rangle = e^{-i\vartheta\hat{O}}|\Psi_t\rangle$. Stated by the so-called quantum Cramér-Rao bound, the best achievable estimation precision by detecting n copies of $|\Psi_t(\vartheta)\rangle$ is lower bounded by $(\Delta\vartheta)^2 \geq 1/[nF_Q(|\Psi_t\rangle, \hat{O})]$. It should be pointed out that implementing the optimal measurement strategy to saturate such a bound is usually challenging. Here, we consider the experimentally feasible observables and show that the corresponding non-optimal detection in estimating ϑ can also witness the QPT.

For a general measurement, the outcomes obeys a ϑ -dependent probability distribution, which determines the maximal information that can be extracted about ϑ , i.e. $(\Delta\vartheta)^2 \geq 1/(nF_C)$, where F_C denotes the Fisher information (FI) and $F_C \leq F_Q[|\Psi_t\rangle, \hat{O}]$. This classical Cramér-Rao bound can be achieved by the maximum likelihood estimation (MLE) for a sufficiently large n [73, 76, 77]. In the explicit example of ANNNI model, we estimate ϑ by suitably choosing to measure the global magnetization $\hat{S}_z = \sum_i \sigma_i^z/2$ [73]. We numerically simulate the estimation uncertainty of ϑ by utilizing the MLE, which is constructed from 50000 measurement outcomes. In order to evaluate the estimation uncertainty $\Delta\vartheta$, namely the fluctuation of the unbiased MLE, we repeat each estimation by 2000 times, from which the distribution of the MLE is obtained in Fig. 2 (f). It can be seen that the MLE near the QPT (corresponding to $\kappa \approx 0.15$) shows a narrower distribution than non-critical cases, directly indicating a better metrological performance achieved by the probe state generated at QCP. In Fig. 2 (g), we further compute the time average of the estimation uncertainty, i.e.

$$\overline{\Delta\vartheta} = \frac{1}{T} \int_0^T \Delta\vartheta \, dt. \quad (8)$$

It clearly exhibits a minimum around the QCP. Hence, the parameter estimation uncertainty achieved by the probe state prepared through non-equilibrium quench dynamics effectively iden-

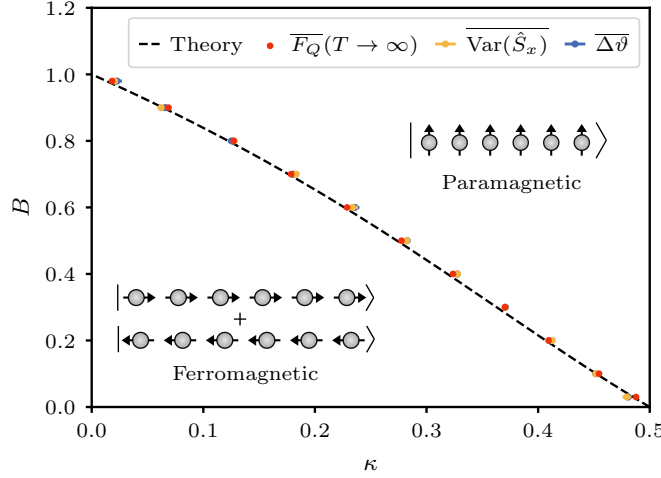


FIG. 3. **Identification of the phase diagram of the ANNNI model.** In the (κ, B) parameter plane of the ANNNI chain, see Eq. (3), we numerically determine the boundary of the phase diagram by finding the maximum of the time-averaged QFI and the global quantum fluctuation [$\Delta = 4.5$ in Eq. (7)], as well as the minimum of the time-averaged phase estimation uncertainty, see Fig. 2. The boundaries obtained based on our dynamical quench-interferometric framework all agree well with the theoretical prediction by the second-order perturbation theory. Here, we set $N = 20$. The $\overline{\text{Var}(\hat{S}_x)}$ and $\overline{\Delta\vartheta}$ are averaged over a finite time window $T = 30$ with a sampling interval $\Delta t = 0.3$ [73].

tifies the QPT.

The feasible detection of quantum phase diagram

The quench-interferometric framework in Fig. 1 establishes a practical routine to identify QPTs. Based on this framework, we next elaborate that the quantum phase diagram can be obtained by sweeping the quenching parameter (κ, B) in the ANNNI Hamiltonian. More specifically, we numerically determines κ_c for each fixed B and then varies B from 0 to 1. In Fig. 3, we depict the phase diagram obtained from the metrological capability quantified by the QFI, the global quantum fluctuations and the phase estimation uncertainty. One can see that the predicted boundary all agrees very well with the theoretical prediction by second-order perturbation theory.

Recently, state-of-the-art quantum simulators have been implemented in a variety of well-controllable many-particle quantum platforms, such as the cold-atom lattice [78–81], the Rydberg-atom array [82–84], and the trapped ion crystal [85, 86], which possess long coherence times, tunable interactions and starts to play significant roles in the simulation of a series of interesting spin models. As an example, we point out that the ANNNI chain considered in this work can be

effectively synthesized using Rydberg atoms [23, 87–90]. Particularly, the fully polarized initial state can be realized with a high fidelity of $\gtrsim 95\%$ [88–90]. The variance and the uncertainty of the MLE estimate can be readily obtained by simple global measurement of the collective spin operators [55, 91–98]. Furthermore, the coherent timescale of this system can reach $\tau \geq 10J^{-1}$, where J represents the strength of the nearest-neighbor interaction. Such a long relevant time scale makes the evaluation of the averaged metrological capability over a time window in our probing framework experimentally feasible. In the Supplementary Materials, we provide a detailed discussion on the operational complexity of the time-averaging requirement [73].

Conclusion & outlook

To summarize, we present a quench-interferometric framework to probe QPTs by introducing the concept of the metrological capability to characterize the post-quenched state, which exhibit a significant peak around the QCP as quantified by the time average of QFI evolution. This framework can be accomplished through globally measuring collective observables to evaluate the quantum fluctuations or the associated estimation uncertainty of the interferometric phase. By taking the chaotic ANNNI model as a representative example, we demonstrate that the QCPs and immediately the phase diagram can be well identified based on such a framework. The scheme is experimentally feasible even with limited measurement resolution of the observables and under the implementation of non-optimal measurement to extract the phase information encoded in the final state. We also demonstrate that our framework can be extended to other QPT Hamiltonians including long-range interacting models as well [73]. Our findings take a step of exploiting quantum metrological concepts and strategies towards the investigation of many-body physics, which heuristically unveils a stimulating interplay between quantum metrology and dynamical quantum criticality [39, 47, 50].

Acknowledgements

The computation is completed in the HPC Platform of Huazhong University of Science and Technology. This work is supported by the National Natural Science Foundation of China (12161141011 and 12174138), the National Key R&D Program of China (2018YFA0306600). Y.-M.C. is also supported by the Young Scientists Fund of the National Natural Science Foundation of China (Grant No. 12304572).

* yaomingchu@hust.edu.cn

† jianmingcai@hust.edu.cn

- [1] S. Sachdev, *Quantum Phase Transitions* (Cambridge University Press, 2011).
- [2] M. Vojta, Quantum phase transitions, [Reports on Progress in Physics](#) **66**, 2069 (2003).
- [3] S. Sachdev, Quantum magnetism and criticality, [Nature Physics](#) **4**, 173 (2008).
- [4] L. Savary and L. Balents, Quantum spin liquids: a review, [Reports on Progress in Physics](#) **80**, 016502 (2016).
- [5] X.-G. Wen, Topological Order: From Long-Range Entangled Quantum Matter to a Unified Origin of Light and Electrons, [International Scholarly Research Notices](#) **2013**, 198710 (2013).
- [6] V. F. Gantmakher and V. T. Dolgoplov, Superconductor–insulator quantum phase transition, [Physics-Uspekhi](#) **53**, 1 (2010).
- [7] J. Zhang, G. Pagano, P. W. Hess, A. Kyprianidis, P. Becker, H. Kaplan, A. V. Gorshkov, Z.-X. Gong, and C. Monroe, Observation of a many-body dynamical phase transition with a 53-qubit quantum simulator, [Nature](#) **551**, 601 (2017).
- [8] I. M. Georgescu, S. Ashhab, and F. Nori, Quantum simulation, [Rev. Mod. Phys.](#) **86**, 153 (2014).
- [9] D. Lv, S. An, Z. Liu, J.-N. Zhang, J. S. Pedernales, L. Lamata, E. Solano, and K. Kim, Quantum Simulation of the Quantum Rabi Model in a Trapped Ion, [Phys. Rev. X](#) **8**, 021027 (2018).
- [10] R. Harris, Y. Sato, A. J. Berkley, M. Reis, F. Altomare, M. H. Amin, K. Boothby, P. Bunyk, C. Deng, C. Enderud, S. Huang, E. Hoskinson, M. W. Johnson, E. Ladizinsky, N. Ladizinsky, T. Lanting, R. Li, T. Medina, R. Molavi, R. Neufeld, T. Oh, I. Pavlov, I. Perminov, G. Poulin-Lamarre, C. Rich, A. Smirnov, L. Swenson, N. Tsai, M. Volkmann, J. Whittaker, and J. Yao, Phase transitions in a programmable quantum spin glass simulator, [Science](#) **361**, 162 (2018).
- [11] A. J. Daley, I. Bloch, C. Kokail, S. Flannigan, N. Pearson, M. Troyer, and P. Zoller, Practical quantum advantage in quantum simulation, [Nature](#) **607**, 667 (2022).
- [12] S.-A. Guo, Y.-K. Wu, J. Ye, L. Zhang, W.-Q. Lian, R. Yao, Y. Wang, R.-Y. Yan, Y.-J. Yi, Y.-L. Xu, *et al.*, A site-resolved two-dimensional quantum simulator with hundreds of trapped ions, [Nature](#) **630**, 613 (2024).
- [13] H.-J. Shao, Y.-X. Wang, D.-Z. Zhu, Y.-S. Zhu, H.-N. Sun, S.-Y. Chen, C. Zhang, Z.-J. Fan, Y. Deng, X.-C. Yao, *et al.*, Antiferromagnetic phase transition in a 3D fermionic Hubbard model, [Nature](#) , 1

- (2024).
- [14] A. Osterloh, L. Amico, G. Falci, and R. Fazio, Scaling of entanglement close to a quantum phase transition, [Nature](#) **416**, 608 (2002).
 - [15] S.-J. Gu, Fidelity approach to quantum phase transitions, [International Journal of Modern Physics B](#) **24**, 4371 (2010).
 - [16] A. Carollo, D. Valenti, and B. Spagnolo, Geometry of quantum phase transitions, [Physics Reports](#) **838**, 1 (2020).
 - [17] J. Arnold, F. Schäfer, A. Edelman, and C. Bruder, Mapping Out Phase Diagrams with Generative Classifiers, [Phys. Rev. Lett.](#) **132**, 207301 (2024).
 - [18] J. Arnold, N. Lörch, F. Holtorf, and F. Schäfer, Machine learning phase transitions: Connections to the Fisher information, [arXiv: 2311.10710](#) (2023).
 - [19] P. Zanardi and N. Paunković, Ground state overlap and quantum phase transitions, [Phys. Rev. E](#) **74**, 031123 (2006).
 - [20] M. Cozzini, R. Ionicioiu, and P. Zanardi, Quantum fidelity and quantum phase transitions in matrix product states, [Phys. Rev. B](#) **76**, 104420 (2007).
 - [21] L. Campos Venuti and P. Zanardi, Quantum Critical Scaling of the Geometric Tensors, [Phys. Rev. Lett.](#) **99**, 095701 (2007).
 - [22] P. Titum, J. T. Iosue, J. R. Garrison, A. V. Gorshkov, and Z.-X. Gong, Probing Ground-State Phase Transitions through Quench Dynamics, [Phys. Rev. Lett.](#) **123**, 115701 (2019).
 - [23] A. Haldar, K. Mallayya, M. Heyl, F. Pollmann, M. Rigol, and A. Das, Signatures of Quantum Phase Transitions after Quenches in Quantum Chaotic One-Dimensional Systems, [Phys. Rev. X](#) **11**, 031062 (2021).
 - [24] M. Heyl, F. Pollmann, and B. Dóra, Detecting Equilibrium and Dynamical Quantum Phase Transitions in Ising Chains via Out-of-Time-Ordered Correlators, [Phys. Rev. Lett.](#) **121**, 016801 (2018).
 - [25] C. B. Dağ, K. Sun, and L.-M. Duan, Detection of Quantum Phases via Out-of-Time-Order Correlators, [Phys. Rev. Lett.](#) **123**, 140602 (2019).
 - [26] C. B. Dağ, P. Uhrich, Y. Wang, I. P. McCulloch, and J. C. Halimeh, Detecting quantum phase transitions in the quasistationary regime of Ising chains, [Phys. Rev. B](#) **107**, 094432 (2023).
 - [27] S. Bandyopadhyay, A. Polkovnikov, and A. Dutta, Late-time critical behavior of local stringlike observables under quantum quenches, [Phys. Rev. B](#) **107**, 064105 (2023).
 - [28] L. G. C. Lakkaraju, S. K. Haldar, and A. Sen(De), Predicting a topological quantum phase transition

- from dynamics via multisite entanglement, [Phys. Rev. A **109**, 022436 \(2024\)](#).
- [29] S. Paul, P. Titum, and M. Maghrebi, Hidden quantum criticality and entanglement in quench dynamics, [Phys. Rev. Res. **6**, L032003 \(2024\)](#).
- [30] X. Nie, B.-B. Wei, X. Chen, Z. Zhang, X. Zhao, C. Qiu, Y. Tian, Y. Ji, T. Xin, D. Lu, and J. Li, Experimental Observation of Equilibrium and Dynamical Quantum Phase Transitions via Out-of-Time-Ordered Correlators, [Phys. Rev. Lett. **124**, 250601 \(2020\)](#).
- [31] C. B. Dağ and K. Sun, Dynamical crossover in the transient quench dynamics of short-range transverse-field Ising models, [Phys. Rev. B **103**, 214402 \(2021\)](#).
- [32] B. Žunkovič, M. Heyl, M. Knap, and A. Silva, Dynamical Quantum Phase Transitions in Spin Chains with Long-Range Interactions: Merging Different Concepts of Nonequilibrium Criticality, [Phys. Rev. Lett. **120**, 130601 \(2018\)](#).
- [33] R. Jafari and A. Akbari, Dynamics of quantum coherence and quantum Fisher information after a sudden quench, [Phys. Rev. A **101**, 062105 \(2020\)](#).
- [34] K. Kobayashi and Y. Motome, Quantum reservoir probing of quantum phase transitions, [arXiv: 2402.07097 \(2024\)](#).
- [35] P. Zanardi, M. G. A. Paris, and L. Campos Venuti, Quantum criticality as a resource for quantum estimation, [Phys. Rev. A **78**, 042105 \(2008\)](#).
- [36] C. Invernizzi, M. Korbman, L. Campos Venuti, and M. G. A. Paris, Optimal quantum estimation in spin systems at criticality, [Phys. Rev. A **78**, 042106 \(2008\)](#).
- [37] M. Mehboudi, L. A. Correa, and A. Sanpera, Achieving sub-shot-noise sensing at finite temperatures, [Phys. Rev. A **94**, 042121 \(2016\)](#).
- [38] M. M. Rams, P. Sierant, O. Dutta, P. Horodecki, and J. Zakrzewski, At the Limits of Criticality-Based Quantum Metrology: Apparent Super-Heisenberg Scaling Revisited, [Phys. Rev. X **8**, 021022 \(2018\)](#).
- [39] Y. Chu, S. Zhang, B. Yu, and J. Cai, Dynamic Framework for Criticality-Enhanced Quantum Sensing, [Phys. Rev. Lett. **126**, 010502 \(2021\)](#).
- [40] X.-Y. Luo, Y.-Q. Zou, L.-N. Wu, Q. Liu, M.-F. Han, M. K. Tey, and L. You, Deterministic entanglement generation from driving through quantum phase transitions, [Science **355**, 620 \(2017\)](#).
- [41] I. Frérot and T. Roscilde, Quantum Critical Metrology, [Phys. Rev. Lett. **121**, 020402 \(2018\)](#).
- [42] Y. Chu, Y. Liu, H. Liu, and J. Cai, Quantum Sensing with a Single-Qubit Pseudo-Hermitian System, [Phys. Rev. Lett. **124**, 020501 \(2020\)](#).
- [43] D.-S. Ding, Z.-K. Liu, B.-S. Shi, G.-C. Guo, K. Mølmer, and C. S. Adams, Enhanced metrology at the

- critical point of a many-body Rydberg atomic system, [Nature Physics](#) **18**, 1447 (2022).
- [44] C. Hotter, H. Ritsch, and K. Gietka, Combining Critical and Quantum Metrology, [Phys. Rev. Lett.](#) **132**, 060801 (2024).
 - [45] D. Braun, G. Adesso, F. Benatti, R. Floreanini, U. Marzolino, M. W. Mitchell, and S. Pirandola, Quantum-enhanced measurements without entanglement, [Rev. Mod. Phys.](#) **90**, 035006 (2018).
 - [46] M. Zhuang, J. Huang, Y. Ke, and C. Lee, Symmetry-protected quantum adiabatic evolution in spontaneous symmetry-breaking transitions, [Annalen der Physik](#) **532**, 1900471 (2020).
 - [47] Y. Chu, X. Li, and J. Cai, Strong Quantum Metrological Limit from Many-Body Physics, [Phys. Rev. Lett.](#) **130**, 170801 (2023).
 - [48] M. Yu, X. Li, Y. Chu, B. Mera, F. N. Ünal, P. Yang, Y. Liu, N. Goldman, and J. Cai, Experimental demonstration of topological bounds in quantum metrology, [National Science Review](#) , nwae065 (2024).
 - [49] H.-L. Shi, X.-W. Guan, and J. Yang, Universal Shot-Noise Limit for Quantum Metrology with Local Hamiltonians, [Phys. Rev. Lett.](#) **132**, 100803 (2024).
 - [50] M. Block, B. Ye, B. Roberts, S. Chern, W. Wu, Z. Wang, L. Pollet, E. J. Davis, B. I. Halperin, and N. Y. Yao, Scalable spin squeezing from finite-temperature easy-plane magnetism, [Nature Physics](#) **20**, 1575 (2024).
 - [51] G. Mihailescu, A. Bayat, S. Campbell, and A. K. Mitchell, Multiparameter critical quantum metrology with impurity probes, [Quantum Science and Technology](#) **9**, 035033 (2024).
 - [52] G. Mihailescu, S. Campbell, and K. Gietka, Uncertain Quantum Critical Metrology: From Single to Multi Parameter Sensing, [arXiv: 2407.19917](#) (2024).
 - [53] M. Adani, S. Cavazzoni, B. Teklu, P. Bordone, and M. G. A. Paris, Critical metrology of minimally accessible anisotropic spin chains, [arXiv: 2405.20296](#) (2024).
 - [54] S. L. Braunstein and C. M. Caves, Statistical distance and the geometry of quantum states, [Phys. Rev. Lett.](#) **72**, 3439 (1994).
 - [55] L. Pezzè, A. Smerzi, M. K. Oberthaler, R. Schmied, and P. Treutlein, Quantum metrology with non-classical states of atomic ensembles, [Rev. Mod. Phys.](#) **90**, 035005 (2018).
 - [56] J. Liu, H. Yuan, X.-M. Lu, and X. Wang, Quantum Fisher information matrix and multiparameter estimation, [Journal of Physics A: Mathematical and Theoretical](#) **53**, 023001 (2019).
 - [57] V. Giovannetti, S. Lloyd, and L. Maccone, Quantum Metrology, [Phys. Rev. Lett.](#) **96**, 010401 (2006).
 - [58] V. Giovannetti, S. Lloyd, and L. Maccone, Advances in quantum metrology, [Nature photonics](#) **5**, 222

(2011).

- [59] D. J. Wineland, J. J. Bollinger, W. M. Itano, and D. J. Heinzen, Squeezed atomic states and projection noise in spectroscopy, [Phys. Rev. A **50**, 67 \(1994\)](#).
- [60] P. Hauke, M. Heyl, L. Tagliacozzo, and P. Zoller, Measuring multipartite entanglement through dynamic susceptibilities, [Nature Physics **12**, 778 \(2016\)](#).
- [61] A. Niezgoda and J. Chwedeńczuk, Many-Body Nonlocality as a Resource for Quantum-Enhanced Metrology, [Phys. Rev. Lett. **126**, 210506 \(2021\)](#).
- [62] Y. Chu, X. Li, and J. Cai, Quantum delocalization on correlation landscape: The key to exponentially fast multipartite entanglement generation, [arXiv: 2404.10973 \(2024\)](#).
- [63] L. Amico, R. Fazio, A. Osterloh, and V. Vedral, Entanglement in many-body systems, [Rev. Mod. Phys. **80**, 517 \(2008\)](#).
- [64] A. Nahum, J. Ruhman, S. Vijay, and J. Haah, Quantum Entanglement Growth under Random Unitary Dynamics, [Phys. Rev. X **7**, 031016 \(2017\)](#).
- [65] D. R. Baykusheva, M. H. Kalthoff, D. Hofmann, M. Claassen, D. M. Kennes, M. A. Sentef, and M. Mitrano, Witnessing Nonequilibrium Entanglement Dynamics in a Strongly Correlated Fermionic Chain, [Phys. Rev. Lett. **130**, 106902 \(2023\)](#).
- [66] M. Gärtner, P. Hauke, and A. M. Rey, Relating Out-of-Time-Order Correlations to Entanglement via Multiple-Quantum Coherences, [Phys. Rev. Lett. **120**, 040402 \(2018\)](#).
- [67] R. J. Lewis-Swan, S. R. Muleady, and A. M. Rey, Detecting Out-of-Time-Order Correlations via Quasiadiabatic Echoes as a Tool to Reveal Quantum Coherence in Equilibrium Quantum Phase Transitions, [Phys. Rev. Lett. **125**, 240605 \(2020\)](#).
- [68] C. Karrasch and D. Schuricht, Dynamical phase transitions after quenches in nonintegrable models, [Phys. Rev. B **87**, 195104 \(2013\)](#).
- [69] V. Alba and M. Fagotti, Prethermalization at Low Temperature: The Scent of Long-Range Order, [Phys. Rev. Lett. **119**, 010601 \(2017\)](#).
- [70] M. Beccaria, M. Campostrini, and A. Feo, Density-matrix renormalization-group study of the disorder line in the quantum axial next-nearest-neighbor Ising model, [Phys. Rev. B **73**, 052402 \(2006\)](#).
- [71] P. Weinberg and M. Bukov, QuSpin: a Python package for dynamics and exact diagonalisation of quantum many body systems part I: spin chains, [SciPost Phys. **2**, 003 \(2017\)](#).
- [72] P. Weinberg and M. Bukov, QuSpin: a Python package for dynamics and exact diagonalisation of quantum many body systems. Part II: bosons, fermions and higher spins, [SciPost Phys. **7**, 020 \(2019\)](#).

- [73] See Supplementary Information for additional details.
- [74] E. Davis, G. Bentsen, and M. Schleier-Smith, Approaching the Heisenberg Limit without Single-Particle Detection, [Phys. Rev. Lett. **116**, 053601 \(2016\)](#).
- [75] F. Fröwis, P. Sekatski, and W. Dür, Detecting Large Quantum Fisher Information with Finite Measurement Precision, [Phys. Rev. Lett. **116**, 090801 \(2016\)](#).
- [76] R. A. Fisher, Theory of statistical estimation, in *Mathematical proceedings of the Cambridge philosophical society*, Vol. 22 (Cambridge University Press, 1925) pp. 700–725.
- [77] S. L. Braunstein, How large a sample is needed for the maximum likelihood estimator to be approximately Gaussian?, [Journal of Physics A: Mathematical and General **25**, 3813 \(1992\)](#).
- [78] I. Bloch, J. Dalibard, and W. Zwerger, Many-body physics with ultracold gases, [Rev. Mod. Phys. **80**, 885 \(2008\)](#).
- [79] I. Bloch, J. Dalibard, and S. Nascimbene, Quantum simulations with ultracold quantum gases, [Nature Physics **8**, 267 \(2012\)](#).
- [80] C. Gross and I. Bloch, Quantum simulations with ultracold atoms in optical lattices, [Science **357**, 995 \(2017\)](#).
- [81] F. Schäfer, T. Fukuhara, S. Sugawa, Y. Takasu, and Y. Takahashi, Tools for quantum simulation with ultracold atoms in optical lattices, [Nature Reviews Physics **2**, 411 \(2020\)](#).
- [82] C. S. Adams, J. D. Pritchard, and J. P. Shaffer, Rydberg atom quantum technologies, [Journal of Physics B: Atomic, Molecular and Optical Physics **53**, 012002 \(2019\)](#).
- [83] A. Browaeys and T. Lahaye, Many-body physics with individually controlled Rydberg atoms, [Nature Physics **16**, 132 \(2020\)](#).
- [84] X. Wu, X. Liang, Y. Tian, F. Yang, C. Chen, Y.-C. Liu, M. K. Tey, and L. You, A concise review of Rydberg atom based quantum computation and quantum simulation*, [Chinese Physics B **30**, 020305 \(2021\)](#).
- [85] R. Blatt and C. F. Roos, Quantum simulations with trapped ions, [Nature Physics **8**, 277 \(2012\)](#).
- [86] C. Monroe, W. C. Campbell, L.-M. Duan, Z.-X. Gong, A. V. Gorshkov, P. W. Hess, R. Islam, K. Kim, N. M. Linke, G. Pagano, P. Richerme, C. Senko, and N. Y. Yao, Programmable quantum simulations of spin systems with trapped ions, [Rev. Mod. Phys. **93**, 025001 \(2021\)](#).
- [87] J. Zeiher, R. Van Bijnen, P. Schauß, S. Hild, J.-y. Choi, T. Pohl, I. Bloch, and C. Gross, Many-body interferometry of a Rydberg-dressed spin lattice, [Nature Physics **12**, 1095 \(2016\)](#).
- [88] H. Labuhn, D. Barredo, S. Ravets, S. De Léséleuc, T. Macrì, T. Lahaye, and A. Browaeys, Tunable

- two-dimensional arrays of single Rydberg atoms for realizing quantum ising models, [Nature](#) **534**, 667 (2016).
- [89] J. Zeiher, J.-y. Choi, A. Rubio-Abadal, T. Pohl, R. van Bijnen, I. Bloch, and C. Gross, Coherent Many-Body Spin Dynamics in a Long-Range Interacting Ising Chain, [Phys. Rev. X](#) **7**, 041063 (2017).
- [90] P. Scholl, H. J. Williams, G. Bornet, F. Wallner, D. Barredo, L. Henriët, A. Signoles, C. Hainaut, T. Franz, S. Geier, A. Tebben, A. Salzinger, G. Zürn, T. Lahaye, M. Weidemüller, and A. Browaeys, Microwave Engineering of Programmable XXZ Hamiltonians in Arrays of Rydberg Atoms, [PRX Quantum](#) **3**, 020303 (2022).
- [91] C. F. Ockeloen, A. F. Tauschinsky, R. J. C. Spreeuw, and S. Whitlock, Detection of small atom numbers through image processing, [Phys. Rev. A](#) **82**, 061606 (2010).
- [92] W. Muessel, H. Strobel, M. Joos, E. Nicklas, I. Stroescu, J. Tomkovič, D. B. Hume, and M. K. Oberthaler, Optimized absorption imaging of mesoscopic atomic clouds, [Applied Physics B](#) **113**, 69 (2013).
- [93] D. B. Hume, I. Stroescu, M. Joos, W. Muessel, H. Strobel, and M. K. Oberthaler, Accurate Atom Counting in Mesoscopic Ensembles, [Phys. Rev. Lett.](#) **111**, 253001 (2013).
- [94] I. Dimitrova, S. Flannigan, Y. K. Lee, H. Lin, J. Amato-Grill, N. Jepsen, I. Čepaitė, A. J. Daley, and W. Ketterle, Many-body spin rotation by adiabatic passage in spin-1/2 XXZ chains of ultracold atoms, [Quantum Science and Technology](#) **8**, 035018 (2023).
- [95] S. Colombo, E. Pedrozo-Penafiel, A. F. Adiyatullin, Z. Li, E. Mendez, C. Shu, and V. Vuletić, Time-reversal-based quantum metrology with many-body entangled states, [Nature Physics](#) **18**, 925 (2022).
- [96] G. Bornet, G. Emperauger, C. Chen, B. Ye, M. Block, M. Bintz, J. A. Boyd, D. Barredo, T. Comparin, F. Mezzacapo, *et al.*, Scalable spin squeezing in a dipolar Rydberg atom array, [Nature](#) **621**, 728 (2023).
- [97] J. Franke, S. R. Muleady, R. Kaubruegger, F. Kranzl, R. Blatt, A. M. Rey, M. K. Joshi, and C. F. Roos, Quantum-enhanced sensing on optical transitions through finite-range interactions, [Nature](#) **621**, 740 (2023).
- [98] S. Imai, G. Tóth, and O. Gühne, Collective Randomized Measurements in Quantum Information Processing, [Phys. Rev. Lett.](#) **133**, 060203 (2024).

Supplementary Materials

Xiangbei Li,¹ Yaoming Chu,^{1,*} Shaoliang Zhang,¹ and Jianming Cai^{1,†}

*¹School of Physics, Hubei Key Laboratory of Gravitation and Quantum Physics,
International Joint Laboratory on Quantum Sensing and Quantum Metrology,
Institute for Quantum Science and Engineering,
Huazhong University of Science and Technology, Wuhan 430074, China*

Supplementary Section

- I. The Emergence of the Peak of the QFI at the Phase Transition Point
- II. Finite-size effect on locating the QPT with time-averaged QFI
- III. Probing the QPT of the ANNNI model under open boundary condition
- IV. Extracting quantum fluctuations with finite measurement resolution
- V. Probing the QPT with parameter estimation uncertainty
- VI. Dynamical quench-interferometric framework for other QPT models
- VII. Efficiency of the quench-interferometric framework

I. The Emergence of the Peak of the QFI at the Phase Transition Point

The connection between the QFI for pure states and the spontaneous symmetry breaking (SSB) associated with QPTs plays a central role in the emergence of a peak of the QFI near the QCP. On the one hand, the QFI for pure states with respect to a unitary parameterization generated by $\hat{\mathcal{O}} = \sum_i \hat{O}_i$ simply reduces to the variance of $\hat{\mathcal{O}}$. For example, the cat state $|\psi\rangle = (|\rightarrow\rangle^{\otimes N} + |\leftarrow\rangle^{\otimes N})/\sqrt{2}$ exhibits an extraordinarily large variance $\text{Var}(\hat{S}_x) = N^2/4$, making it particularly advantageous for quantum metrology. On the other hand, SSB does not actually occur for finite system sizes, causing the ground state to become a macroscopic superposition of the symmetry-broken states. As a result, the variance of the order parameter $\hat{\mathcal{O}}$ in the symmetry-broken phase becomes extremely large in the ground state, scaling quadratically with the system size [1, 2].

Taking the ANNNI chain as an illustrative example, the ANNNI chain in thermodynamic limit exhibits a spontaneous Z_2 (with $U = \prod_{i=1}^N \sigma_i^z$) symmetry breaking in the ferromagnetic phase, with the corresponding order parameter $\hat{\mathcal{O}} = \hat{S}_x$. As shown in the inset of Fig. S1 (a), the spin Husimi Q distribution of the ground state in the ferromagnetic phase clearly demonstrates that it is a macroscopic superposition of two symmetry-broken states, resulting in a large variance of \hat{S}_x . We choose the initial state as $|\Psi_0\rangle = |\uparrow\rangle^{\otimes N}$, which is the symmetric ground state deep in the paramagnetic phase. The time-evolved state $|\Psi_t\rangle$ will preserve the symmetry, ensuring the order parameter as zero during the time evolution, i.e., $\langle\Psi_t|\hat{\mathcal{O}}|\Psi_t\rangle = 0$. Therefore, the QFI of $|\Psi_t\rangle$ corresponding to $\hat{\mathcal{O}}$ becomes

$$\begin{aligned} F_Q(|\Psi_t\rangle, \hat{\mathcal{O}}) &= 4 \left[\langle\Psi_t|\hat{\mathcal{O}}^2|\Psi_t\rangle - \langle\Psi_t|\hat{\mathcal{O}}|\Psi_t\rangle^2 \right] = 4 \langle\Psi_t|\hat{\mathcal{O}}^2|\Psi_t\rangle \\ &= 4 \sum_{i,j} e^{-i(E_i-E_j)t} \langle E_i|\Psi_0\rangle \langle\Psi_0|E_j\rangle \langle E_j|\hat{\mathcal{O}}^2|E_i\rangle. \end{aligned} \quad (\text{S.1})$$

where $\{|E_i\rangle\}$ represents the eigenstates of the Hamiltonian. The long-time average

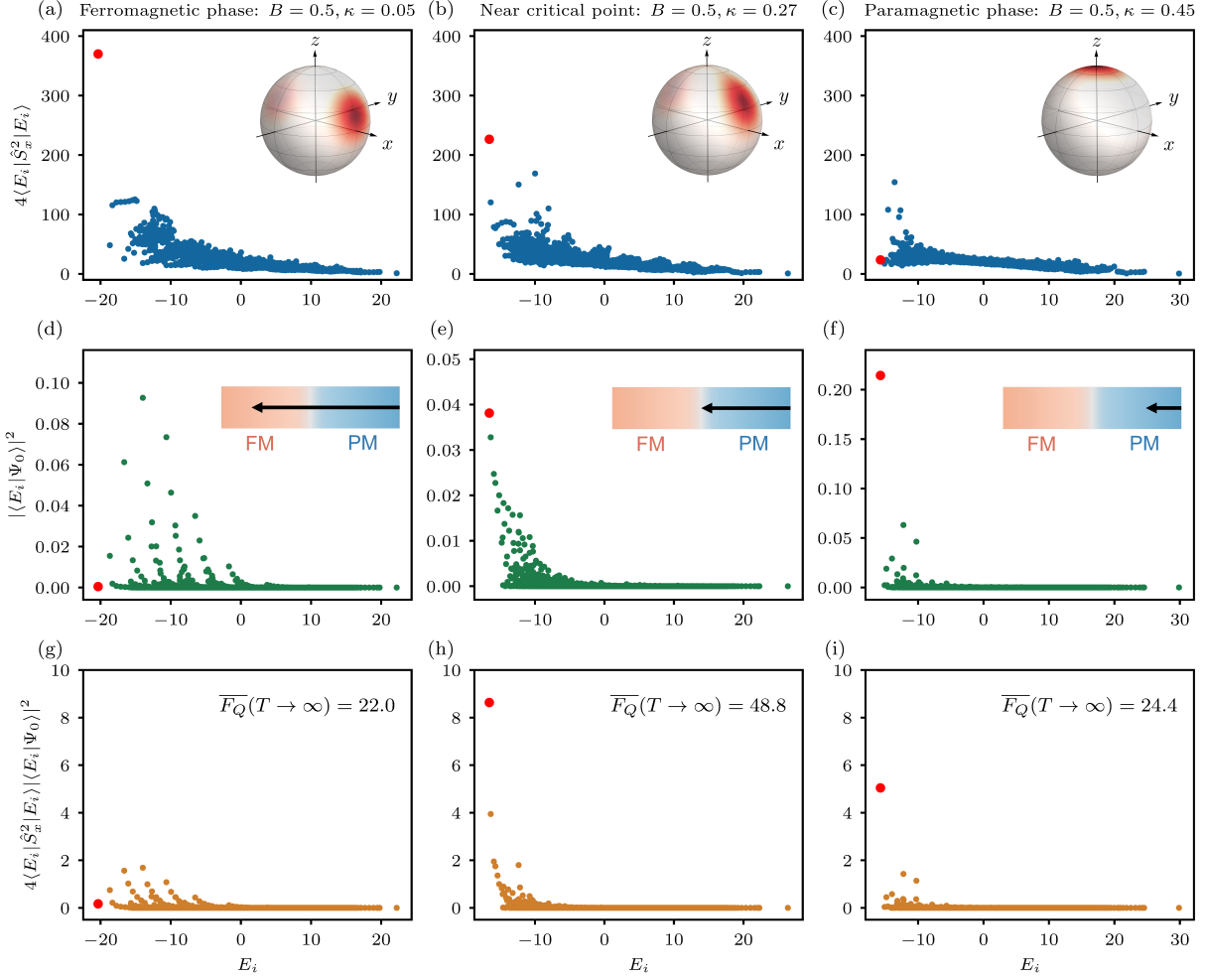


FIG. S1. The time-averaged QFI is determined by two factors: the variance $4 \langle E_i | \hat{S}_x^2 | E_i \rangle$ and the population $|\langle E_i | \Psi_0 \rangle|^2$. In the insets of (a-c), we plot the spin Husimi Q distribution of the ground state in different phases and near the QCP. Panels (d-f) show the population of the system's eigenstates after quantum quenches to different parameters. Panels (g-i) show the quantity $4 \langle E_i | \hat{S}_x^2 | E_i \rangle |\langle E_i | \Psi_0 \rangle|^2$. Results corresponding to the ground state are highlighted with red dots. All the calculations are performed for a system size of $N = 20$.

of the QFI is then

$$\begin{aligned}
 \overline{F_Q}(T \rightarrow \infty) &= \lim_{T \rightarrow \infty} \frac{1}{T} \int_0^T F_Q(|\Psi_t\rangle, \hat{\mathcal{O}}) dt = 4 \sum_i |\langle E_i | \Psi_0 \rangle|^2 \langle E_i | \hat{\mathcal{O}}^2 | E_i \rangle \\
 &= 4 \sum_i |\langle E_i | \Psi_0 \rangle|^2 \langle E_i | \hat{S}_x^2 | E_i \rangle.
 \end{aligned} \tag{S.2}$$

As can be seen, the $\overline{F_Q}$ is determined by two parts, i.e. the population of the eigenstates of the quench Hamiltonian ($|\langle E_i | \Psi_0 \rangle|^2$) and the variance of order parameter in those eigenstates ($\langle E_i | \hat{S}_x^2 | E_i \rangle$).

Next, as shown in Fig. S1, we qualitatively analyze the behavior of $\overline{F_Q}$ in three scenarios: (i) In the ferromagnetic phase, the variance of the ground state is extremely large, see panel (a). However, the quench crossing the critical point mainly drives the system into highly excited eigenstates that only have small variance of the order parameter, as shown in panel (d), resulting in small value of the averaged QFI. This is because that the ground states of the paramagnetic and ferromagnetic Hamiltonians are radically different, leading to that the initial state is a high-temperature state with respect to the ferromagnetic Hamiltonian. (ii) When the quenched Hamiltonian remains in the paramagnetic phase, main population will still stay in the ground and low excited states, see panel (f). For example, one can see a significant overlap between the initial state and the ground state. Nevertheless, the disordered paramagnetic phase lacks long-range order and $\text{Var}(\hat{S}_x)$ (especially in the ground state) is small, as shown in panel (c). (iii) In the vicinity of the QCP, the initial state remains a relatively low-temperature state with respect to the critical Hamiltonian. Combined with long-range order and thus relatively large $\langle E_i | \hat{S}_x^2 | E_i \rangle$ in the ground and low-lying excited states, a unique peak of the averaged QFI occurs around the QCP, see panels (b), (e) and (h).

Based on the above physical picture on the emergence of the QFI peak, we point out that our framework might also be applied to a variety of quantum critical models including long-range interacting QPT systems without finite-temperature spontaneous symmetry breaking (thus without finite-temperature order) [2–7]. In Sec. VI (D) and Fig. S9, we verify this picture by using the long-range Ising model [5–7] as a representative example. For long-range interacting QPT systems with finite-

temperature order, we remark that our approach might also be valid as long as the temperature of the symmetric ground state of the disordered Hamiltonian with respect to the quenched ordered Hamiltonian is larger than the critical temperature, above which the long-range order is absent [2, 4, 5, 8].

II. Finite-Size Effect on Locating the QPT with Time-Averaged QFI

To explore the influence of finite-size effect, we calculate the time-averaged QFI for different system sizes. The corresponding results are shown in Fig. S2. It can be seen that our method can effectively locate the QCP even using systems of relatively small sizes. As the system size increase from $N = 8$ to $N = 20$, the location of achieving the maximum \overline{F}_Q , denoted as $\kappa = \kappa_{\max}$, move towards the critical point κ_c predicted by second-order perturbation theory.

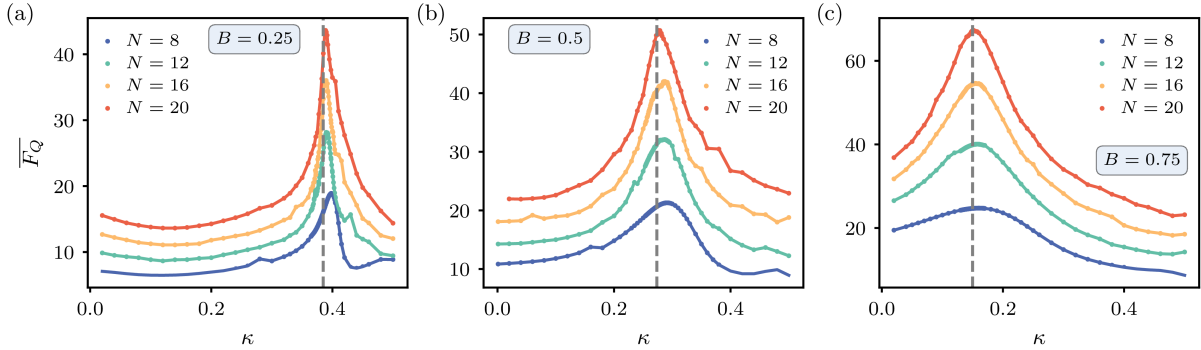


FIG. S2. Time-averaged QFI [see Eq. (S.2)] of ANNNI model plotted as functions of κ for different system sizes. We choose the parameter B as 0.25, 0.5, 0.75 in panels (a-c) respectively. The vertical dashed lines indicate the critical point κ_c predicted by second-order perturbation theory.

III. Probing the QPT of the ANNNI Model under Open Boundary Condition

In this section, we consider the quench dynamics of the ANNNI model with open boundary condition. Due to the lack of translational symmetry, we utilize the time-evolving block decimation (TEBD) method [9–11] in this case. We compute the

time-averaged QFI for two different system size, $N = 24$ and $N = 30$ spins. We fix the parameter B at 0.25, 0.5, 0.75 and then vary κ . In order to guarantee the accuracy of the results, we restrict our calculations of the QFI evolution to $T = 30$ for $N = 24$ and $T = 15$ for $N = 30$. As can be seen in Fig. S3, while the finite size effect is more pronounced under the open boundary condition, the time-averaged QFI still displays prominent peaks near the critical point, implying the robustness of our findings with respect to the open boundary condition.

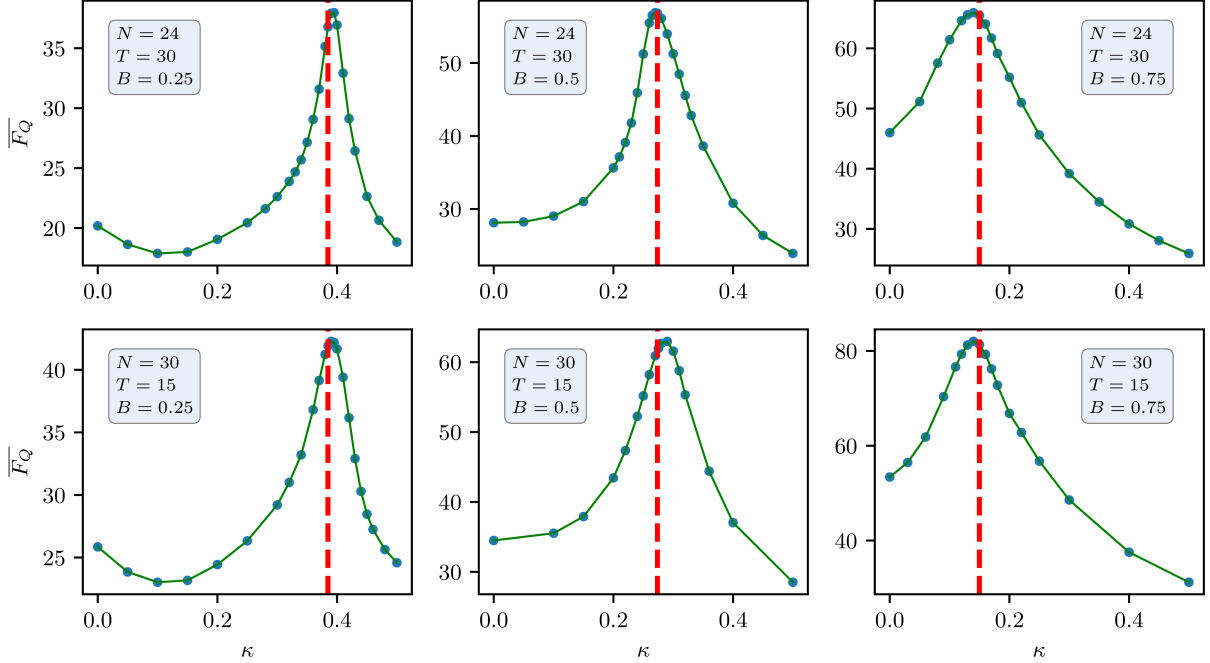


FIG. S3. TEBD results for ANNNI chain under open boundary conditions with $N = 24$ and $N = 30$ spins. The time-averaged QFI is plotted as functions of κ with B fixed at 0.25, 0.5, and 0.75. We note the time-averaging window is $T = 30$ for $N = 24$ and $T = 15$ for $N = 30$. The vertical dashed lines mark the critical point κ_c of the corresponding B predicted by second-order perturbation theory [12].

IV. Extracting Quantum Fluctuations with Finite Measurement Resolution

In the main text, we propose to repeatedly measure the collective observable $\hat{S}_x =$

$\sum_i \sigma_i^x / 2 = \sum_{S_x} S_x \hat{\Pi}_{S_x}$ to extract its quantum fluctuation. Here, S_x represents the eigenvalue of \hat{S}_x and $\hat{\Pi}_{S_x}$ is the corresponding projection operator. To model the imperfect detection with finite resolution, we replace the ideal probabilities $P(S_x) = \langle \Psi_t | \hat{\Pi}_{S_x} | \Psi_t \rangle$ with a smeared probability density [13]

$$P_{\text{dn}}(S'_x) = \sum_{S_x} P(S'_x | S_x) P(S_x), \quad (\text{S.3})$$

where $P(S'_x | S_x)$ is a convolution function representing the probability to obtain the result S'_x when the actual value is S_x . Typically, this function is modeled as a normalized Gaussian $P(S'_x | S_x) = e^{-(S'_x - S_x)^2 / (2\Delta^2)} / (\sqrt{2\pi}\Delta)$, where the parameter Δ quantifies the measurement resolution. This approach aligns with the model for coarse-grained detectors described in Ref. [14], which assumes a continuous measurement

$$\hat{\Pi}(S'_x) = \frac{1}{\sqrt{2\pi}\Delta} e^{-(S'_x - \hat{S}_x)^2 / (2\Delta^2)} = \sum_{S_x} \frac{1}{\sqrt{2\pi}\Delta} e^{-(S'_x - S_x)^2 / (2\Delta^2)} \hat{\Pi}_{S_x}. \quad (\text{S.4})$$

This measurement return to the perfect measurement $\hat{\Pi}(S'_x) = \delta(S'_x - \hat{S}_x)$ for $\Delta \rightarrow 0$.

V. Probing the QPT with Parameter Estimation Uncertainty

(A) *Selection of the Positive Operator-Valued Measurement (POVM).*— To effectively detect QPTs, the phase encoding and the subsequent measurement strategy must capture the underlying metrological capability of the input quantum states. By noticing the large variance of $\hat{\mathcal{O}} = \hat{S}_x$ with respect to the post-quenched state $|\Psi_t\rangle$ near the QCP, we choose the collective spin operator \hat{S}_x as the phase encoding operator, namely $|\Psi_t(\vartheta)\rangle = e^{-i\vartheta\hat{S}_x}\Psi_t$. According to Heisenberg's uncertainty principle, measuring the conjugate operator \hat{S}_z is often a suitable choice to extract the phase. Therefore, we consider the global measurement $\hat{S}_z = \sum_i \sigma_i^z / 2 = \sum_{S_z} S_z \hat{\Pi}_{S_z}$ in the main text to estimate the unknown phase shift ϑ encoded in the multi-spin state

$|\Psi_t(\vartheta)\rangle$, where S_z denotes the eigenvalue of \hat{S}_z and $\hat{\Pi}_{S_z}$ is the corresponding projection operator. Firstly, we demonstrate that the Fisher information extracted by this simple global measurement can reach the QFI as $\vartheta \rightarrow 0$ and exhibits nearly synchronous dynamics as the QFI when ϑ is small. Specifically, the Fisher information associated with the measurement of \hat{S}_z is given by

$$F_C = \sum_{S_z} P(S_z|\vartheta) \left(\frac{\partial \ln P(S_z|\vartheta)}{\partial \vartheta} \right)^2, \quad (\text{S.5})$$

where $P(S_z|\vartheta) = \langle \Psi_t(\vartheta) | \hat{\Pi}_{S_z} | \Psi_t(\vartheta) \rangle$ is the probability of obtaining the outcome of S_z . Generally, F_C depends on the value of the parameter ϑ . In Fig. S4 (a), we plot how F_C varies with ϑ for $B = 0.75$, $\kappa = 0.15$ and $t = 7.5$. We observe that F_C is significantly enhanced and approaches the QFI (F_Q) when $\vartheta = n\pi$ with n taking the value of integers. In Fig. S4 (b), we present the time evolution of F_C for different values of ϑ and compare these results to F_Q . The results show that when ϑ is small, F_C is very close to F_Q and show strongly correlated behaviors. Moreover,

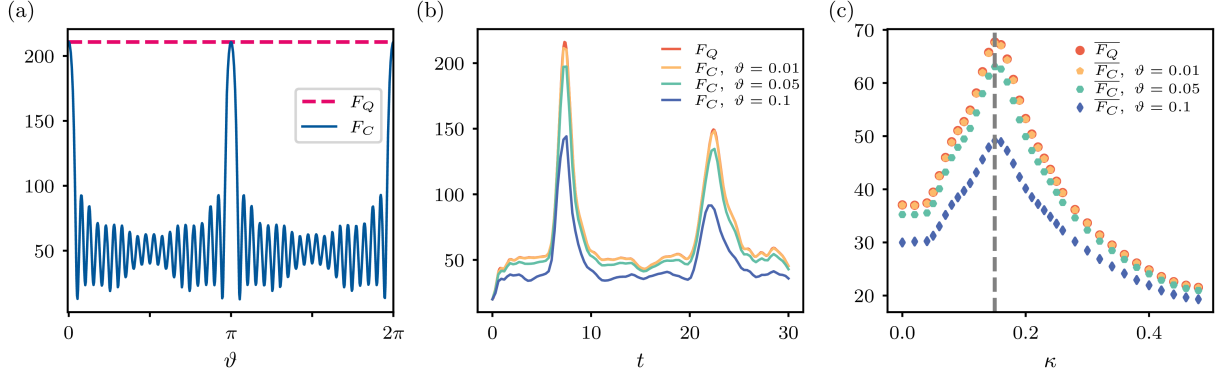


FIG. S4. (a) The Fisher information associated with the measurement of \hat{S}_z as a function of the phase ϑ at the evolution time $t = 7.5$. (b) Time evolution of F_C for different values of ϑ . (c) Time-averaged QFI ($\overline{F_Q}$) and FI ($\overline{F_C}$) plotted as functions of κ over a time window of $T = 15$. The vertical dashed line indicates the critical point of $\kappa_c \approx 0.15$. Here, the system parameters of the ANNNI model are set as $\kappa = 0.15 \approx \kappa_c$ in panels (a-b) and $B = 0.75$ in all panels. All the calculations are performed for a system size of $N = 20$.

we calculate the time-averaged QFI and FI over a time window of $T = 15$, denoted by $\overline{F_Q}$ and $\overline{F_C}$ respectively. The results are shown in Fig. S4 (c). It is evident that $\overline{F_C}$ also exhibits distinct peaks near the critical point, indicating that the QPT can be successfully detected by non-optimized metrological measurement to extract the phase ϑ .

In order to evaluate the robustness of POVM selection in detecting QCPs, we consider the measurement of a global spin operator that deviates from \hat{S}_z , i.e., $\hat{S}_{\hat{n}} = \cos \alpha \hat{S}_z + \sin \alpha \hat{S}_x$ with $\alpha = \pi/20$. The corresponding results are presented in Fig. S5. While this measurement is never optimal—namely, it does not reach the QFI for any ϑ , as shown in Fig. S5 (a)—the time-averaged FI still exhibits a peak near the QCP. This effectively demonstrates the robustness of the POVM selection in detecting QPTs.

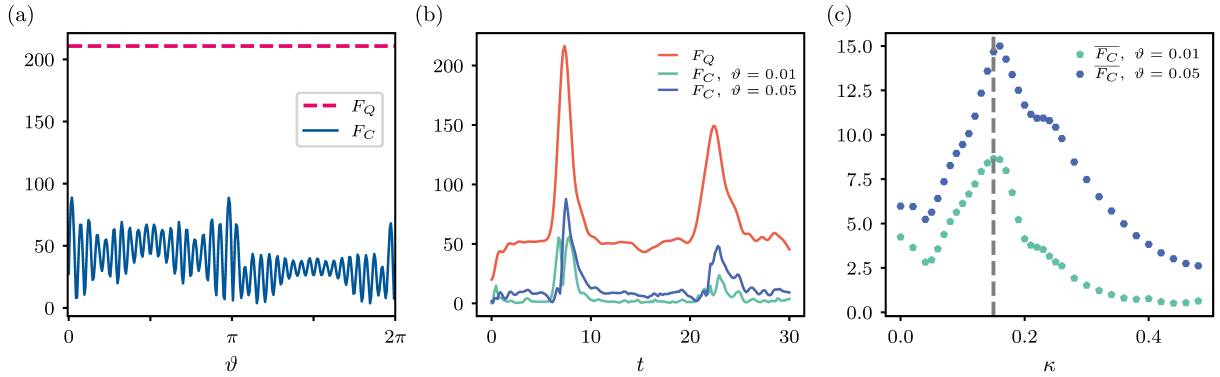


FIG. S5. (a) The Fisher information as a function of the phase ϑ at $t = 7.5$, based on the measurement $\hat{S}_{\hat{n}} = \cos \alpha \hat{S}_z + \sin \alpha \hat{S}_x$ with $\alpha = \pi/20$. (b) Time evolution of F_C for different values of ϑ . (c) Time-averaged FI ($\overline{F_C}$) as functions of κ over a time window of $T = 15$. The vertical dashed line marks the critical point $\kappa_c \approx 0.15$. The system parameters are consistent with Fig. S4, with $\kappa = 0.15 \approx \kappa_c$ in (a-b) and $B = 0.75$ in all panels. All the calculations are performed for a system size of $N = 20$.

(B) *Maximum Likelihood Estimation (MLE).*— In order to unbiasedly estimate the phase ϑ from the measurement outcomes, we consider the approach of maximum

likelihood estimation (MLE). Taking the measurement of \hat{S}_z as an example, and assuming that the outcomes on n copies of the parameterized quantum state $|\Psi_t(\vartheta)\rangle$ as $\{S_z^{(i)}\}_{i=1}^n = \{S_z^{(1)}, S_z^{(2)}, \dots, S_z^{(n)}\}$, the log-likelihood function is then defined as

$$l(\vartheta; \{S_z^{(i)}\}_{i=1}^n) = \sum_{i=1}^n \ln P(S_z^{(i)}|\vartheta), \quad (\text{S.6})$$

where $P(S_z^{(i)}|\vartheta)$ denotes the probability of obtaining the outcome $S_z^{(i)}$. We numerically calculate the log-likelihood function $l(\vartheta; \{S_z^{(i)}\}_{i=1}^n)$ over a range that covers the possible values of the unknown phase ϑ and find its maximum point within this range. MLE estimate corresponds to the value of ϑ that achieves the maximum of the log-likelihood function [15].

VI. Dynamical quench-interferometric framework for other QPT models

(A) *Probing the QPT of the transverse field Ising chain.*— The transverse field Ising chain is one of the most studied models in quantum phase transitions [16, 17]. Its Hamiltonian is given by

$$H(B) = - \sum_i \sigma_i^x \sigma_{i+1}^x - B \sum_i \sigma_i^z. \quad (\text{S.7})$$

This model represents the noninteracting limit ($\kappa = 0$) of the ANNNI Hamiltonian [see Eq. (3) of the main text] and it exhibits a quantum phase transition at $B_c = 1$ from a ferromagnetic phase ($B < 1$) to a paramagnetic phase ($B > 1$). We propose to prepare the spin chain in a fully polarized initial state $|\Psi\rangle = |\uparrow\rangle^{\otimes N}$, and let it evolve under the quenched Hamiltonian $H(B)$. The time-averaged QFI $\overline{F_Q} = \int_0^T F_Q(|\Psi_t\rangle, \hat{S}_x) dt$, calculated over a time window of $T = 30$, is plotted as a function of the quench parameter B in Fig. S6. It can be seen that the $\overline{F_Q}$ is considerably enhanced near the critical point.

(B) *Probing the QPT of the XY chain.*— The Hamiltonian of the XY chain [18] is

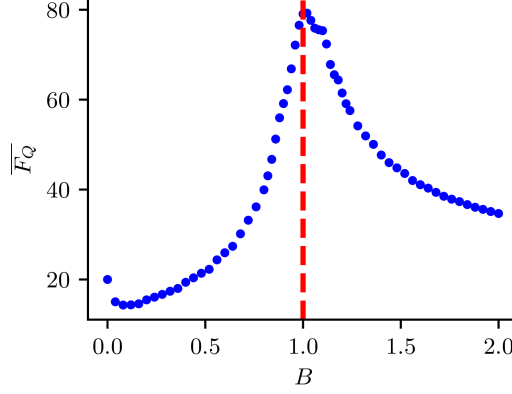


FIG. S6. Time-averaged QFI for the transverse Ising chain. The vertical dashed lines mark the critical point $B_c = 1$. Here the system size is set to $N = 20$, and the time-averaging window is $T = 30$.

given by

$$H(B) = -J_x \sum_i \sigma_i^x \sigma_{i+1}^x - J_y \sum_i \sigma_i^y \sigma_{i+1}^y - B \sum_i \sigma_i^z. \quad (\text{S.8})$$

Without loss of generality, we assume that $J_x \geq |J_y| \geq 0$ (thus $J_x + J_y > 0$). The system undergoes transitions from paramagnetic phase to ferromagnetic phase at $B = \pm(J_x + J_y)$. We assume to initialize the spin chain in a fully polarized state $|\Psi\rangle = |\uparrow\rangle^{\otimes N}$ and let it evolve under the quenched Hamiltonian $H(B)$. The time-averaged QFI $\overline{F_Q} = \int_0^T F_Q(|\Psi_t\rangle, \hat{S}_x) dt$, calculated over a time window of $T = 30$, is plotted as a function of the quench parameter B in Fig. S6. We choose $J_x = 1, J_y = 0.4$ for Fig. S7 (a) and $J_x = 1, J_y = 0.8$ for Fig. S7 (b). It is evident that $\overline{F_Q}$ is significantly enhanced near the critical point.

(C) *Probing QPT of the Ising chain with transverse and longitudinal fields.*— The Hamiltonian of the antiferromagnetic Ising chain with both transverse and longitudinal fields [19–21] is written as

$$H(B_x, B_z) = \sum_i \sigma_i^z \sigma_{i+1}^z - B_x \sum_i \sigma_i^x - B_z \sum_i \sigma_i^z. \quad (\text{S.9})$$

This is a nonintegrable model and exhibits two phases at zero temperature [19, 20],

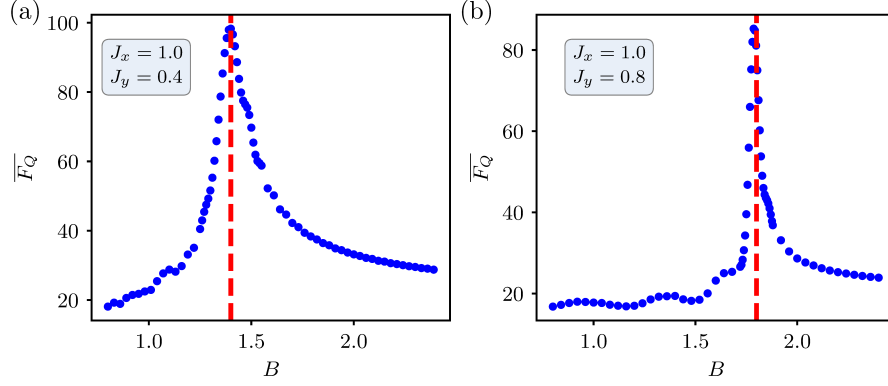


FIG. S7. Time-averaged QFI for the XY chain. Here the system size is set to $N = 20$, and the averaging time window is $T = 30$. The vertical dashed lines mark the critical points at $B_c = 1.4$ for (a) and $B_c = 1.8$ for (b) respectively.

namely an antiferromagnetic phase for weak fields, and a paramagnetic phase for strong fields. These phases are separated by a second-order phase transition [see the dashed line in Fig. S8 (b)].

Similarly, we assume that the spin chain is initialized in a polarized state $|\Psi\rangle = |\rightarrow\rangle^{\otimes N}$ and consider the evolution governed by $H(B_x, B_z)$. The time-averaged QFI, $\overline{F_Q} = \int_0^T F_Q(|\Psi_t\rangle, \hat{O}) dt$, is computed by choosing the generator of the unitary interferometer as $\hat{O} = \sum_i (-1)^i \sigma_i^z / 2$. To probe the antiferromagnetic to paramagnetic quantum phase transition at a fixed value of B_x , we fix the quench parameter B_x and vary B_z . For example, we show the results for B_x fixed at 0.437 in Fig. S8, where the vertical dashed line marks the critical point, $(B_z)_c$, from Ref. [19] obtained by the DMRG calculation. It can be seen that the position where $\overline{F_Q}$ reaches the maximum coincides with the critical $(B_z)_c$. In Fig. S8 (b), we further present the critical points estimated from the maximum of the time-averaged $\overline{F_Q}$ for various B_x . These results are in good agreement with the phase boundaries determined by the DMRG calculation.

(D) *Probing the QPT of the long-range transverse-field Ising chain.*— We investigate

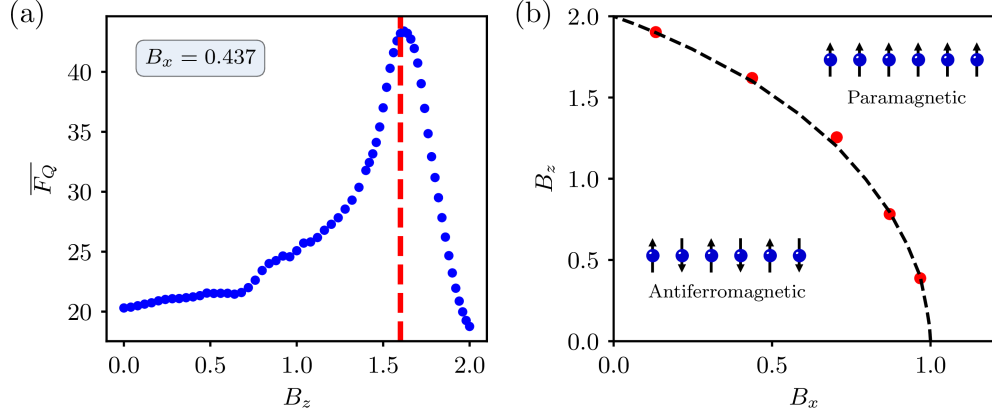


FIG. S8. (a) Time-averaged QFI plotted as a function of B_z when fixing $B_x = 0.437$. The vertical dashed line marks the critical point, $(B_z)_c$, predicted from the DMRG calculation. (b) Phase diagram in the parameter plane of (B_x, B_z) . The phase boundary is well described by locating the peak of the time-averaged QFI over a window of $T = 30$ (red dots). The dashed line is the critical line from Ref. [19] calculated using DMRG. Here the system size is set as $N = 20$.

the long-range transverse-field Ising chain [5–7, 22, 23] described by the Hamiltonian

$$H = -J \sum_{i < j} \frac{\sigma_i^x \sigma_j^x}{|i - j|^\alpha} - B \sum_i \sigma_i^z, \quad (\text{S.10})$$

where $B > 0$ is the transverse-field strength and $J > 0$ controls the spin-spin coupling that decays with a power-law scaling. For convenience, we set $B = 1$. The model exhibits two quantum phases: a paramagnetic phase for small J and a Z_2 symmetry-broken ferromagnetic phase for large J . Here, we focus on the case of $\alpha = 3$, which is proven to lack finite-temperature long-range order by stronger versions of the Mermin-Wagner theorem [3], and thus is a representative example of QPT systems without finite-temperature spontaneous symmetry breaking. Ref. [7] determined the critical point as $J_c \approx 0.70$ for $B = 1$ and $\alpha = 3$ using linked-cluster expansions. This critical point was also validated by numerical results obtained through exact diagonalization [6], DMRG calculations [22], and quantum Monte

Carlo simulations [23].

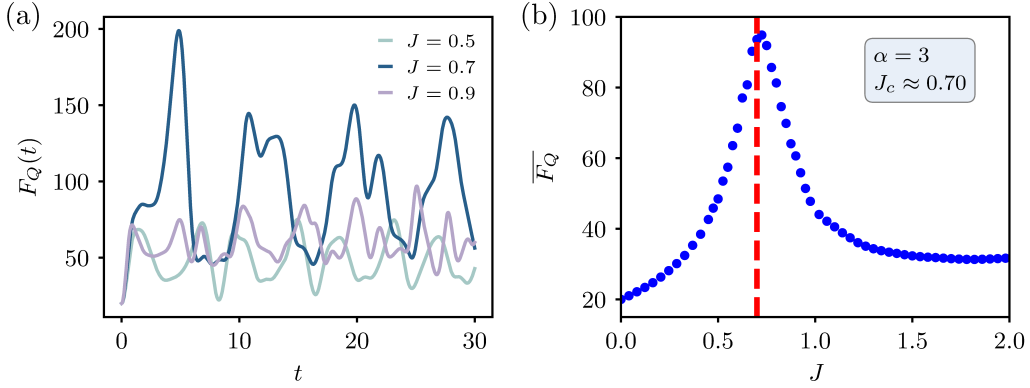


FIG. S9. (a) The QFI dynamics for different values of J with $B = 1$ and $\alpha = 3$. The significantly enhanced QFI (dark blue curve) corresponds to the quench parameter J close to the QCP. (b) Time-averaged QFI plotted as a function of J . Here, the system size is set to $N = 20$, and the time-averaging window is $T = 30$. The vertical dashed line indicates the critical point $J_c \approx 0.70$ determined by linked-cluster expansions [7].

We assume to initialize the spin chain in a fully polarized state $|\Psi\rangle = |\uparrow\rangle^{\otimes N}$ and let it evolve under the quenched Hamiltonian described in Eq. (S.10). As shown in Fig. S9 (a), the dynamics of the QFI, $F_Q(t) = F_Q(|\Psi_t\rangle, \hat{S}_x)$, exhibit a significant enhancement near the QCP compared to scenarios away from it. The time-averaged QFI $\overline{F_Q} = \int_0^T F_Q(t) dt$, calculated over a time window of $T = 30$, is plotted as a function of the parameter J in Fig. S9 (b). It is evident that $\overline{F_Q}$ displays a peak in the vicinity of the critical point. We also remark that our framework might also be extended to higher-dimensional cases if $\alpha > 2D$, where D denotes the spatial dimension of the system [3, 23, 24].

VII. Efficiency of the quench-interferometric framework

(A) *The experimental complexity.*— Here, we demonstrate that the experimental complexity of our method grows polynomially with system size N . For the one-

dimensional short-range interaction model considered in our work, the celebrated Lieb–Robinson bound suggests that the evolution time grows linearly with system size N to allow the relevant many-body dynamics—such as the buildup of correlations and fluctuations near the critical point—to manifest [25–27]. This is also confirmed by our numerical results, see Fig. S10. Consequently, the time-averaging window should scale linearly with system size N . We note that for long-range interacting or higher-dimensional systems, the buildup of correlations is faster, thus requiring even less time [27–31]. Since our method only requires global measurements of the collective spin operators to obtain the variance of the generator or the MLE uncertainty, the number of measurements required at each time step only needs to scale linearly with N to ensure accuracy. Therefore, the overall complexity of our method is at most polynomial in system size N , ensuring its efficiency.

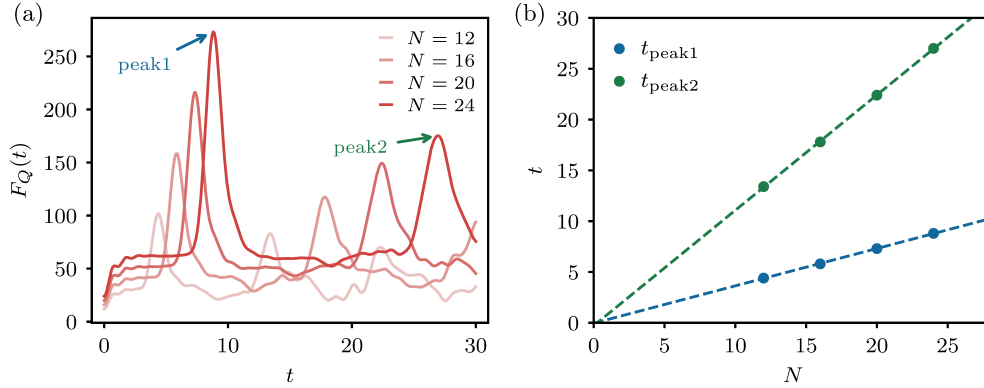


FIG. S10. (a) Time evolution of $F_Q(t)$ for different system sizes of N , ranging from 12 to 24. The arrows highlight two peaks that emerge in the evolution of $F_Q(t)$. It can be seen that as N increases, $F_Q(t)$ takes longer time to develop the same peak. (b) The times at which these peaks occur, denoted by t_{peak1} and t_{peak2} , are plotted as functions of N . The dashed lines represent linear fits to the data. The system parameters of the ANNNI model are set to $B = 0.75, \kappa = 0.15$.

(B) *The time-averaging operation.*— To obtain time-averaged quantities over a time

window T , we discretize the time window into $n + 1$ equally spaced time points $\{t_i\}$ with $t_0 = 0$, $t_n = T$ and a sampling interval $\Delta t = T/n$. For each time point t_i , the system is evolved under the quench Hamiltonian H for a duration t_i , resulting in the evolved state $|\Psi_{t_i}\rangle = e^{-iHt_i} |\Psi_0\rangle$. We then use the evolved state $|\Psi_{t_i}\rangle$ to extract the desired quantities. To obtain quantities like the quantum fluctuation of the generator or the uncertainty of MLE, repeated measurements are required. Therefore, for each time point t_i , we should repeat the above process multiple times. Once all time points $\{t_i\}$ are completed, the time-averaged quantity \bar{A} is approximated as

$$\bar{A} = \frac{1}{n+1} \sum_{i=0}^n A(t_i), \quad (\text{S.11})$$

where \bar{A} represents the time-averaged quantity, and $A(t_i)$ represents the measured value of the quantity A at time t_i .

(C) *Determining the time-averaging window.*— Here, we propose a practical experimental strategy to determine a suitable length for the time-averaging window. By selecting a series of measurement times, i.e., $\{t_i = i\Delta t\}$ with a suitably chosen Δt and $i = 0, 1, \dots, n$, the time-averaged quantity up to t_n can be obtained according to Eq. (S.11), which we denote as $\bar{A}_n = \bar{A}(t_n)$. In actual implementations, the final value of n can be determined by the convergence behavior of the averaged \bar{A}_n . Specifically, once we obtain $A(t_n)$ at the time t_n , we can update the values of \bar{A} from \bar{A}_{n-1} to \bar{A}_n . When the sequence $\{\bar{A}_0, \bar{A}_1, \dots, \bar{A}_n\}$ tends to stabilize and converge, we set the final averaging time as $T = n\Delta t$.

As shown in Fig. S11 (a), we plot the time-averaged QFI $\overline{F_Q}(T)$ as a function of the time window T . It can be seen from the figure that, under the corresponding parameters, $\overline{F_Q}(T)$ tends to stabilize for $T \geq 15$. Beyond this time, one can see that the position of the time-averaged QFI peak is robust against changes in the length of the time-averaging window, as shown in Fig. S11 (b), where we examine different time windows $T = 20, 40$ and 60 , and compare these results with the

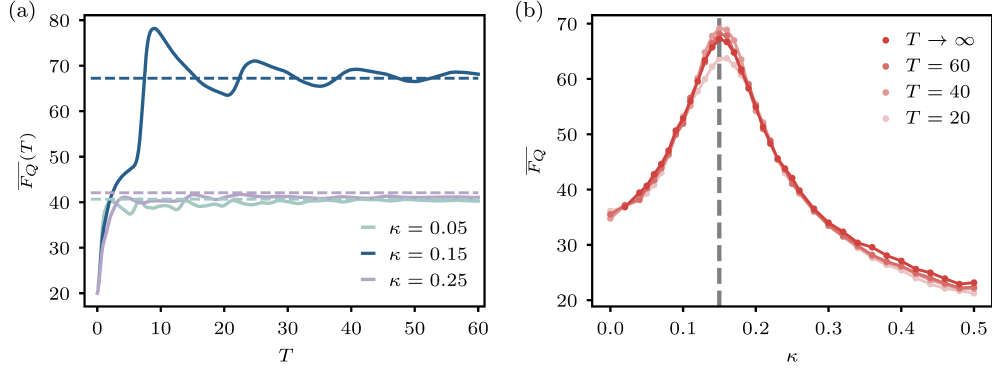


FIG. S11. (a) Time-averaged QFI plotted as a function of the time window T for $B = 0.75$ and $\kappa = 0.05, 0.15, 0.25$. The horizontal dashed line represents the results of $\overline{F_Q}$ for $T \rightarrow \infty$ calculated using Eq. (S.2). (b) Time-averaged QFI plotted as a function of κ for different time windows, with $B = 0.75$. The vertical dashed line marks the critical point $\kappa_c \approx 0.15$. All the calculations are performed for a system size of $N = 20$.

limit as $T \rightarrow \infty$ calculated according to Eq. (S.2). These results demonstrate the feasibility of our framework in experiments with limited time-averaging windows.

* yaomingchu@hust.edu.cn

† jianmingcai@hust.edu.cn

- [1] T. Abad and V. Karimipour, Scaling of macroscopic superpositions close to a quantum phase transition, [Phys. Rev. B **93**, 195127 \(2016\)](#).
- [2] M. Block, B. Ye, B. Roberts, S. Chern, W. Wu, Z. Wang, L. Pollet, E. J. Davis, B. I. Halperin, and N. Y. Yao, Scalable spin squeezing from finite-temperature easy-plane magnetism, [Nature Physics **20**, 1575 \(2024\)](#).
- [3] P. Bruno, Absence of Spontaneous Magnetic Order at Nonzero Temperature in One- and Two-Dimensional Heisenberg and XY Systems with Long-Range Interactions, [Phys. Rev. Lett. **87**, 137203 \(2001\)](#).
- [4] N. Defenu, T. Donner, T. Macrì, G. Pagano, S. Ruffo, and A. Trombettoni, Long-range

- interacting quantum systems, [Rev. Mod. Phys. **95**, 035002 \(2023\)](#).
- [5] A. Dutta and J. K. Bhattacharjee, Phase transitions in the quantum Ising and rotor models with a long-range interaction, [Phys. Rev. B **64**, 184106 \(2001\)](#).
 - [6] M. Knap, A. Kantian, T. Giamarchi, I. Bloch, M. D. Lukin, and E. Demler, Probing Real-Space and Time-Resolved Correlation Functions with Many-Body Ramsey Interferometry, [Phys. Rev. Lett. **111**, 147205 \(2013\)](#).
 - [7] S. Fey and K. P. Schmidt, Critical behavior of quantum magnets with long-range interactions in the thermodynamic limit, [Phys. Rev. B **94**, 075156 \(2016\)](#).
 - [8] E. G. Lazo, M. Heyl, M. Dalmonte, and A. Angelone, Finite-temperature critical behavior of long-range quantum Ising models, [SciPost Phys. **11**, 076 \(2021\)](#).
 - [9] G. Vidal, Efficient Classical Simulation of Slightly Entangled Quantum Computations, [Phys. Rev. Lett. **91**, 147902 \(2003\)](#).
 - [10] G. Vidal, Efficient Simulation of One-Dimensional Quantum Many-Body Systems, [Phys. Rev. Lett. **93**, 040502 \(2004\)](#).
 - [11] J. Hauschild and F. Pollmann, Efficient numerical simulations with Tensor Networks: Tensor Network Python (TeNPy), [SciPost Phys. Lect. Notes , 5 \(2018\)](#).
 - [12] M. Beccaria, M. Campostrini, and A. Feo, Density-matrix renormalization-group study of the disorder line in the quantum axial next-nearest-neighbor Ising model, [Phys. Rev. B **73**, 052402 \(2006\)](#).
 - [13] L. Pezzè, A. Smerzi, M. K. Oberthaler, R. Schmied, and P. Treutlein, Quantum metrology with nonclassical states of atomic ensembles, [Rev. Mod. Phys. **90**, 035005 \(2018\)](#).
 - [14] F. Fröwis, P. Sekatski, and W. Dür, Detecting Large Quantum Fisher Information with Finite Measurement Precision, [Phys. Rev. Lett. **116**, 090801 \(2016\)](#).
 - [15] R. A. Fisher, Theory of statistical estimation, in *Mathematical proceedings of the Cambridge philosophical society*, Vol. 22 (Cambridge University Press, 1925) pp. 700–725.
 - [16] S. Sachdev, *Quantum Phase Transitions* (Cambridge University Press, 2011).
 - [17] S. Suzuki, J.-i. Inoue, and B. K. Chakrabarti, *Quantum Ising phases and transitions in transverse Ising models*, Vol. 862 (Springer, 2012).
 - [18] A. Dutta, G. Aeppli, B. K. Chakrabarti, U. Divakaran, T. F. Rosenbaum, and D. Sen,

Quantum Phase Transitions in Transverse Field Spin Models: From Statistical Physics to Quantum Information (Cambridge University Press, 2015).

- [19] A. A. Ovchinnikov, D. V. Dmitriev, V. Y. Krivnov, and V. O. Cheranovskii, Antiferromagnetic Ising chain in a mixed transverse and longitudinal magnetic field, [Phys. Rev. B **68**, 214406 \(2003\)](#).
- [20] J. Simon, W. S. Bakr, R. Ma, M. E. Tai, P. M. Preiss, and M. Greiner, Quantum simulation of antiferromagnetic spin chains in an optical lattice, [Nature **472**, 307 \(2011\)](#).
- [21] O. F. d. A. Bonfim, B. Boechat, and J. Florencio, Ground-state properties of the one-dimensional transverse Ising model in a longitudinal magnetic field, [Phys. Rev. E **99**, 012122 \(2019\)](#).
- [22] Z. Zhu, G. Sun, W.-L. You, and D.-N. Shi, Fidelity and criticality of a quantum Ising chain with long-range interactions, [Phys. Rev. A **98**, 023607 \(2018\)](#).
- [23] J. A. Koziol, A. Langheld, S. C. Kapfer, and K. P. Schmidt, Quantum-critical properties of the long-range transverse-field Ising model from quantum Monte Carlo simulations, [Phys. Rev. B **103**, 245135 \(2021\)](#).
- [24] S. Fey, S. C. Kapfer, and K. P. Schmidt, Quantum criticality of two-dimensional quantum magnets with long-range interactions, [Phys. Rev. Lett. **122**, 017203 \(2019\)](#).
- [25] E. H. Lieb and D. W. Robinson, The finite group velocity of quantum spin systems, [Communications in Mathematical Physics **28**, 251 \(1972\)](#).
- [26] S. Bravyi, M. B. Hastings, and F. Verstraete, Lieb-Robinson Bounds and the Generation of Correlations and Topological Quantum Order, [Phys. Rev. Lett. **97**, 050401 \(2006\)](#).
- [27] Y. Chu, X. Li, and J. Cai, Strong Quantum Metrological Limit from Many-Body Physics, [Phys. Rev. Lett. **130**, 170801 \(2023\)](#).
- [28] P. Hauke and L. Tagliacozzo, Spread of Correlations in Long-Range Interacting Quantum Systems, [Phys. Rev. Lett. **111**, 207202 \(2013\)](#).
- [29] P. Richerme, Z.-X. Gong, A. Lee, C. Senko, J. Smith, M. Foss-Feig, S. Michalakis, A. V. Gorshkov, and C. Monroe, Non-local propagation of correlations in quantum systems with long-range interactions, [Nature **511**, 198 \(2014\)](#).
- [30] J. Eisert, M. van den Worm, S. R. Manmana, and M. Kastner, Breakdown of Quasilo-

- cality in Long-Range Quantum Lattice Models, [Phys. Rev. Lett. **111**, 260401 \(2013\)](#).
- [31] A. Y. Guo, M. C. Tran, A. M. Childs, A. V. Gorshkov, and Z.-X. Gong, Signaling and scrambling with strongly long-range interactions, [Phys. Rev. A **102**, 010401 \(2020\)](#).